

An NMPC-ECBF Framework for Dynamic Motion Planning and Execution in vision-based Human-Robot Collaboration

Dianhao Zhang, Mien Van, Pantelis Sopasakis, Seán McLoone, *Senior Member, IEEE*

arXiv:2304.06923v3 [cs.RO] 19 Aug 2023

Abstract—To enable safe and effective human–robot collaboration (HRC) in smart manufacturing, seamless integration of sensing, cognition, and prediction into the robot controller is critical for real-time awareness, response, and communication inside a heterogeneous environment (robots, humans, and equipment). The proposed approach takes advantage of the prediction capabilities of nonlinear model predictive control (NMPC) to execute safe path planning based on feedback from a vision system. In order to satisfy the requirement of real-time path planning, an embedded solver based on a penalty method is applied. However, due to tight sampling times, NMPC solutions are approximate, and hence the safety of the system cannot be guaranteed. To address this we formulate a novel safety-critical paradigm with an exponential control barrier function (ECBF) used as a safety filter. We also design a simple human–robot collaboration scenario using V-REP to evaluate the performance of the proposed controller and investigate whether integrating human pose prediction can help with safe and efficient collaboration. The robot uses OptiTrack cameras for perception and dynamically generates collision-free trajectories to the predicted target interactive position. Results for a number of different configurations confirm the efficiency of the proposed motion planning and execution framework. It yields a 19.8% reduction in execution time for the HRC task considered.

Note to Practitioners—This research addresses the need to improve the efficiency of human–robot interactions in practical collaborative robotics applications. Existing approaches typically alternate between robot and human actions leading to long cycle times. This limits the applicability of collaborative robots in manufacturing environments. Our approach to addressing this problem is to (1) employ a motion capture system to track the movement of the human co-worker in the shared workspace; (2) apply machine learning tools to process the motion data to anticipate the co-worker’s future motion and intended action; (3) exploit a control framework and advanced numerical optimization tools that can take advantage of this predictive information to generate and continually update the robot’s trajectory in real-time to efficiently execute the desired action while avoiding collisions, and; (4) incorporate an additional safety layer within the control framework to compensate for inevitable numerical and prediction errors that arise, thereby ensuring the safety of the co-worker. In this way the robot is able to take actions in parallel with the human operator, which minimizes the idle time of both agents compared with conventional perception-based HRC, thereby enabling a substantial reduction in the execution time of HRC tasks.

Index Terms—Non-linear Model Predictive Control, Embedded path planning, Safe Human–robot Collaboration, OptiTrack, Safety-critical Control

The authors are with the Centre for Intelligent Autonomous Manufacturing Systems (i-AMS), School of Electronics, Electrical Engineering and Computer Science, Queen’s University Belfast, Belfast BT9 5AG, U.K. E-mail: dzhang07, m.van, p.sopasakis, s.mcloone@qub.ac.uk.

I. INTRODUCTION

With the advancements in technologies of motion prediction and embedded path planning, accurate and online human–robot collaboration (HRC) has been rapidly developed in smart manufacturing [1], [2]. The learning space for executing human–robot collaboration tasks with a flexible joint manipulator is quite large and the dynamics are, in general, nonlinear, time-varying, and complex. Safe and smooth HRC is still an open challenge particularly for autonomous systems navigating in shared spaces with humans (e.g. intra-logistic and service robotics) and in densely crowded environments [3], [4]. For these scenarios, it is necessary to develop robots with the ability to understand the ongoing task, accurately detect the human’s position and infer upcoming steps based on human demonstrations [5].

Vision-based human action recognition and motion prediction are crucial problems in a HRC system [6]. Action recognition aims to classify the categories of a human’s current dynamics. To activate a robot at the proper time, the estimated classification category can be used as a prior condition for motion prediction. Motion prediction is concerned with forecasting future body movements and poses based on observations of past movements, and can be used to improve the collaboration efficiency in HRC [7]. Estimates of the future evolution of body poses can be used to define both the target position for the robot end-effector and the dynamic obstacles (body parts) for collision avoidance. In our work, an OptiTrack camera is adopted to achieve high-performance optical tracking combined with wearable devices in order to obtain a streaming skeletal representation of the human body. This data is then used as input to the task recognition and motion prediction modules.

Safety regulations ISO 10218 and the technical specification ISO 15066 [8] must be adhered to if a robot is deployed in a shared working environment with a human. These define cooperative robot operation as being contact type (e.g. power and force limiting (PFL), hand guiding (HG)) or non-contact type (e.g. safety-rated monitored stop (SRMS), speed and separation monitoring (SSM)) interactions. In this work, we consider the design of a control framework for SSM-based non-contact HRC, which guarantees safety by remaining a safe distance from humans during interactions.

We employ a model predictive control (MPC) based control system to meet the safety standards and process the online feedback from a vision system. Since the HRC environment is

dynamic and stochastic, and cannot be fully predicted a priori, MPC has become more and more popular in motion planning because it can handle various kinds of kinematic and dynamic constraints [9], [10]. The nonlinear model predictive control (NMPC) law is computed by solving a nonlinear optimal control problem online, taking into account a kinematic model. In [11], NMPC is adopted to solve the task-constrained motion planning problem. Considering safety in physical human-robot interaction (pHRI), [12] proposes an online NMPC method using a kinematic model based on feedback from a vision system.

If solved accurately, NMPC can guarantee asymptotic stability and collision avoidance [13]. However, numerical methods cannot return a perfectly accurate solution, especially within the stringent sampling time requirements we often encounter in robotics (typically a few milliseconds). This presents challenges for the real-time computation of NMPC as there is the potential for collisions if an accurate solution cannot be computed within the available time [14]. To overcome this limitation when the system is controlled by NMPC only, it is necessary to calculate the minimum distance between the end-effector and a human's interactive body component more accurately and to add a safety filter to constrain the robot behavior within a safe area. To solve this problem, we use the Gilbert-Johnson-Keerth (GJK) algorithm [15] to solve the collision detection problem and add a control barrier function (CBF) based constraint into the NMPC problem to guarantee the safety of the operator. In [16], a CBF-based approach is presented to constrain a redundant manipulator within a safe working area when interacting with a human operator. High-order CBF (HOCBF) and exponential CBF (ECBF) extensions are proposed in [17], [18] to solve higher-order relative degree problems. In this paper, we combine a vision system with NMPC-ECBF to solve the safe pHRI problem online.

In summary, the existing research gaps are as follows. Firstly, there is no established approach for designing a safe controller that uses the information from human motion prediction. Secondly, collaboration under a tight-sampling regime limits the accuracy of the NMPC solver, leading to errors that may present a risk to the human operators in the shared workspace.

With estimates of the future target and obstacle position in the working environment, we propose a real-time motion planning algorithm for the physical human-robot interaction (pHRI) task based on NMPC-ECBF. In this work, to test the performance of the proposed controller, we set up a HRC scenario with a 7 degrees of freedom (DOF) manipulator (a Baxter robot) whereby motion capture, action recognition, motion prediction, and trajectory planning modules are integrated into a single system. The scenario, a screw-driver usage task, is divided into a sequence of sub-tasks with the robot end-effector required to reach a continuously updated predicted interactive position without collision when a sub-task is triggered. However, as human motion and pose predictions are subject to approximation errors, the risk of collision still exists in HRC. Therefore, the output configuration of a manipulator is followed by a safety-critical controller implemented using an ECBF-based approach.

There have been several works [19] which consider integrating motion prediction into HRC tasks, but no corresponding safe controllers have been proposed to guarantee the safety of human operators. In this work, we not only perform path planning based on the predicted human motion but also develop a safety filter following the NMPC path planner to enhance the safety of human operators and ensure satisfaction of the ISO safety regulation. This makes the approach applicable to real-world manufacturing.

The main contributions of the paper are as follows:

(1) We integrate human motion predictions as piecewise targets into a robot motion planner to achieve seamless HRC, which reduces the idle time for agents in HRC compared with the existing HRC models in manufacturing [20].

(2) Since the trajectory generated by NMPC has the potential for collision because the solver only solves the first-order optimality conditions and does not guarantee a global optimum we employ an ECBF to enforce constraint satisfaction and collision avoidance while taking advantage of the path planning properties of NMPC.

(3) We develop a real-life human-robot collaboration scenario to test the safety and efficiency of the proposed human motion prediction enhanced HRC control methodology.

This paper is organized as follows: Section II describes the overall HRC system. Related work is introduced in Section III. The formulations and derivations of the target problem are presented in Section IV. Section V discusses the methodology for solving the problem, consisting of formulations for the system, obstacles detection, introduction to the NMPC algorithm and the solver used in the optimization problem. The controller design is introduced in Section VI. Then, Section VII describes the experimental setup and presents the results of the simulations conducted to evaluate the performance of the proposed NMPC-ECBF based control solution for human-robot collaboration. Finally, Section VIII gives the conclusions.

Notation: The following notation is used throughout the paper. Let \mathbb{R} , \mathbb{R}_+ , \mathbb{R}^n , $\mathbb{R}^{m \times n}$ and \mathbb{N} denote the sets of real numbers, the sets of positive real numbers, the set of real vectors of length n , the set of m by n real matrices and non-negative integers, respectively. Let x , \mathbf{x} , and \mathbf{X} denote scalar, vector and matrix quantities, respectively, \mathcal{X} a set, and X a constant. For any non-negative integers $k_1 < k_2$ the finite set $\{k_1, \dots, k_2\}$ is denoted by $\mathbb{N}_{[k_1, k_2]}$. For $\mathbf{x} \in \mathbb{R}^n$, $[\mathbf{x}]_+ = \max\{0, \mathbf{x}\}$ is defined element wise.

II. OVERALL SYSTEM DESIGN

The overall design of the collision-free HRC system is shown in Fig 1. The proposed HRC system consists of motion capture, action recognition, motion prediction, decision-making, path planning, and robot controller modules. The motion capture module relies on OptiTrack cameras to generate high-quality 3D streaming skeleton pose estimates at a sampling rate of 20 frames per second. Using recorded spatial-temporal data for a human performing task-related motions/activities as training data, a motion prediction module is pretrained to predict the future one-second evolution of

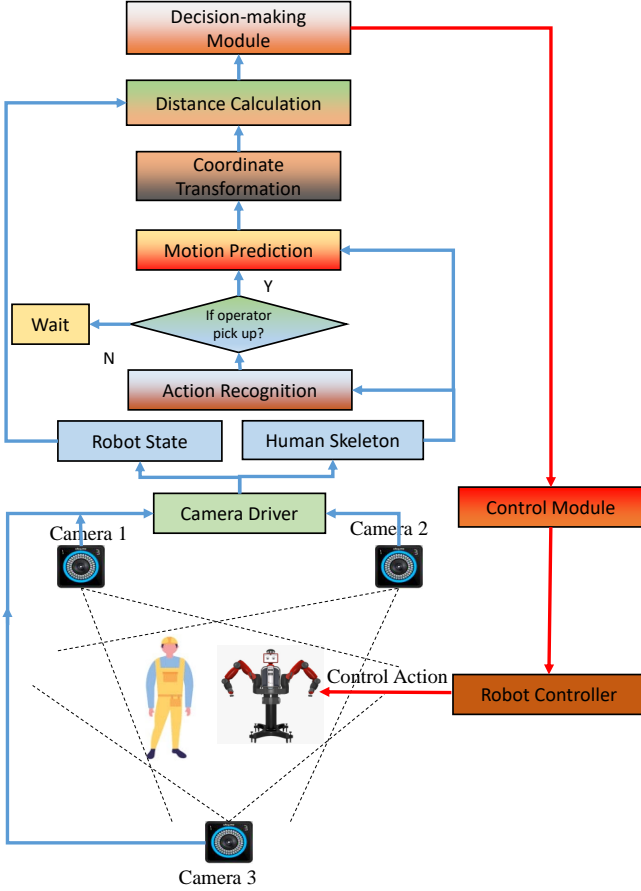


Figure 1: Proposed human-robot collaboration system design

human poses (20 frames) based on the motion observed over the previous one-second interval. The decision-making module is implemented using NMPC-ECBF based motion planning and robot execution mechanisms. In our work, a robot starts from a random position in the working environment and continuously searches for a collision-free path to the estimated interaction coordinates based on the received 1-second ahead pose estimation feedback provided by the predictor module.

III. RELATED WORKS

A. Methods to solve trajectory optimization in MPC

When the system is linear, the constraints are affine and the cost functions are quadratic, the associated MPC optimization problem is a quadratic program. Several convex optimization algorithms have been proposed [21], [22] which are fast, robust and possess global convergence guarantees. When the system is modeled by nonlinear equations with non-convex constraints, sequential quadratic programming (SQP) [21], and interior point (IP) methods [23] are widely used to solve constrained nonconvex problems. To implement the real-time iteration scheme, several software packages such as MUSCOD-II [24] and ACADO [25] have been proposed based on the SQP algorithm. In contrast to the first-order approaches mentioned above, Newton-type methods are able to deal with general constraints and have faster rates of convergence [26]. This leads to a considerable reduction in computation time

and makes them better suited to handling real-time nonlinear problems.

The proximal averaged Newton-type method for optimal control (PANOC) is applied for optimal control considering obstacle avoidance [27], which was proposed in [28]. Compared with SQP and IP, PANOC does not require the solution of linear systems or quadratic programming problems at every iteration and it involves only very simple operations such as vector additions, and scalar and inner products. Additionally, PANOC is able to converge globally to a point that satisfies the first-order optimality conditions of the problem from any initial guess. As an extension, [29], [30] combines the proximal averaged Newton-type method for optimal control (PANOC) with the penalty and augmented Lagrangian methods to compute approximate stationary points of non-convex problems.

We note that although MPC is widely used in practice, it is known that suboptimality and infeasibility due to the numerical optimization method can compromise the stability and positive invariance (satisfaction of constraints) properties of the MPC-controlled system. There have been a few works such as [31] that attempt to remedy this issue, but these are limited to linear dynamical systems, convex formulations, and specific numerical optimization methods. To the best of the authors' knowledge no results exist on the problem of NMPC stability under inexact numerical optimization. In this work we focus on the issue of collision avoidance, and we demonstrate that the combination of nonlinear MPC, PANOC, and a CBF-based framework leads to a significant improvement in safety in terms of obstacle avoidance.

B. Safety-critical Manipulator Control

A system is commonly defined to be safe when its state never leaves some chosen set, known as the safety set. This forms the basis of controlled invariance [32], that is, finding a control strategy that ensures the system always remains in the safety set. In [32], a safety filter is used in the control of a nonlinear system to restrict the desired inputs in a way that ensures safety of the system when necessary. The method proposed in [33] formulates robust control Lyapunov and barrier functions to provide guarantees of stability and safety in the presence of model uncertainty. A control barrier function (CBF) is applied in our work to solve the collision avoidance problem. Applications of the CBF approach to the control of a redundant manipulator can be found in [34], [35].

IV. PROBLEM FORMULATION

Formally, the skeleton-format input to the action recognition and motion prediction modules is represented by 3D joint positions of m joints for a sequence of frames recorded over time, which is the same format as in [36]. The action pose at time (frame) t is $\mathbf{p}(t) \in \mathbb{R}^{3m}$. The observed time length is $t \in [1, \tau_o]$ and the unobserved time length is $t \in [\tau_o+1, \tau_o+\tau_p]$ for prediction.

For a single human action sequence belonging to a set of N_a possible actions, $\mathcal{A} = \{1, \dots, N_a\}$, we have the observed and future motion matrices, \mathbf{P}_{prev} and \mathbf{P}_{fut} , where $\mathbf{P}_{\text{prev}} = [\mathbf{p}(1), \dots, \mathbf{p}(\tau_o)] \in \mathbb{R}^{\tau_o \times 3m}$ and $\mathbf{P}_{\text{fut}} = [\dot{\mathbf{p}}(\tau_o +$

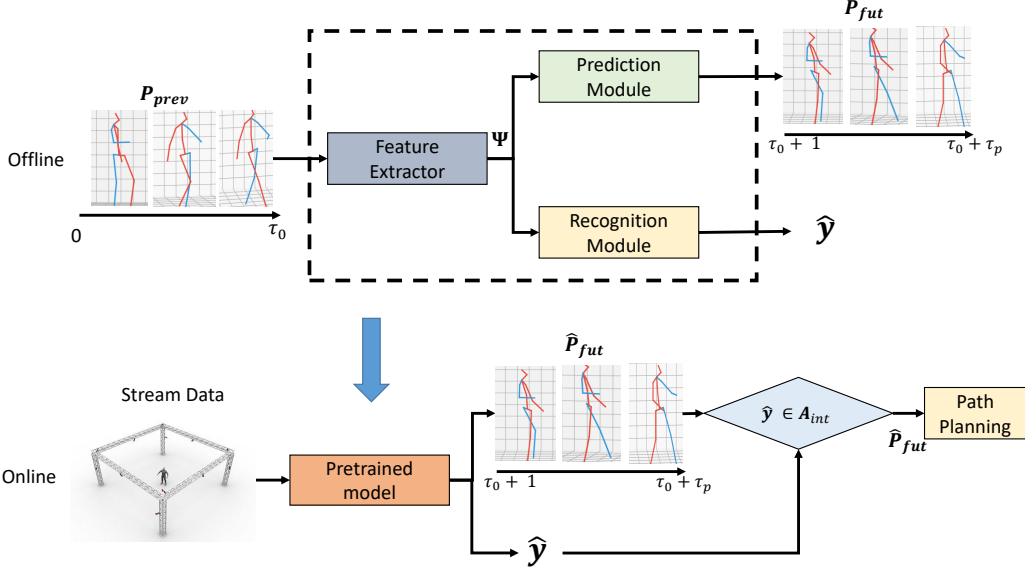


Figure 2: Work flow from non-local graph convolution (NGC) based vision system to path planning. The outputs from the recognition and prediction modules are estimated human action category and future pose sequence, respectively.

$1), \dots, \hat{p}(\tau_0 + \tau_p)] \in \mathbb{R}^{\tau_p \times 3m}$ and the action classification label encoded as a one-hot vector $\hat{y} \in \{0, 1\}^{N_a}$. The predicted human pose at time t is denoted as $\hat{p}(t) \in \mathbb{R}^{3m}$, which can be divided into the right hand's position $\hat{p}_{rh}(t) \in \mathbb{R}^3$ as the target position for the robot and the remaining body joints' positions $\hat{p}_o(t) \in \mathbb{R}^{3(m-1)}$ to decide the positions of obstacles.

Human action recognition and motion prediction are achieved using the two stage deep learning computer vision approach introduced in [36], as depicted in Fig. 2. The 3D-skeleton data stream provided by the OptiTrack motion capture system is firstly processed by a bidirectional LSTM and a GCN architecture incorporating the attention mechanism to extract spatial-temporal features of the human motion dynamics. The generated feature map, denoted as Ψ , is then fed simultaneously to two modules, one that performs prediction and one that performs recognition. The motion prediction task is achieved using an LSTM based decoder, while the action recognition task is performed using a CNN followed by conditional random fields (CRF). Initially the models are trained offline using collected HRC task samples. Following training, streaming data is fed to the model, to generate the predicted future pose sequence \hat{P}_{fut} and predicted action category \hat{y} . Denoting the feature extraction, motion prediction and action recognition functions within the Deep Neural Network model as f_{ext} , f_{pred} and f_{recg} , respectively, and θ_{ext} , θ_{pred} and θ_{recg} as their trainable parameters, the extracted feature map Ψ , the estimated future motion \hat{P}_{fut} and one-hot vector class category \hat{y} can be expressed as

$$\Psi = f_{ext}(P_{prev}; \theta_{ext}), \quad (1a)$$

$$\hat{P}_{fut} = f_{pred}(\Psi; \theta_{pred}), \quad (1b)$$

$$\hat{y} = f_{recg}(\Psi; \theta_{recg}). \quad (1c)$$

If the predicted action is one that requires robot interaction,

the predicted final position of the right hand (denoted $\hat{p}_{rh}(\tau_p)$) is set as the target interactive position for the robot end-effector and the predicted final position of the other joints are set as the center of capsule-format obstacles.

Given the previous human motion sequence P_{prev} and the initial position of the robot arm holding the screw for the screw-driver usage task, and assuming that: (1) the dynamics of the manipulator are known; and (2) the uncertainties in the system can be neglected, the objective is to determine a torque input τ_{act} to the robot, which enables the robot to track the predicted position of the human's right hand $\hat{p}_{rh}(t)$ to the target position and to present the screw to the human operator with a specific pose, while at all times avoiding collision with the human's body.

Denoting the set of interactive human actions requiring robot interaction as \mathcal{A}_{int} , where $\mathcal{A}_{int} \subset \mathcal{A}$, the motion prediction and path planning tasks are triggered if the predicted HRC task $\hat{y} \in \mathcal{A}_{int}$, as shown in Fig. 1.

V. NMPC MOTION PLANNING SCHEME

A. System Description

To model the n -DOF robotic manipulator (chosen as the right arm of our Baxter robot) with joint positions $q \in \mathbb{R}^n$, we consider an input-affine nonlinear system of the form

$$\dot{\chi} = f(\chi) + g(\chi)\tau, \quad (2)$$

where $\chi = [q, \dot{q}] \in \mathbb{R}^{2n}$ is the state of the system and $\tau \in \mathbb{R}^n$ is the control input. Functions $f : \mathbb{R}^{2n} \rightarrow \mathbb{R}^{2n}$ and $g : \mathbb{R}^{2n} \rightarrow \mathbb{R}^{2n \times n}$ are continuously differentiable in χ .

Consider an n -degrees-of-freedom manipulator with equations of motion defined as

$$M(q)\ddot{q} + C(q, \dot{q})\dot{q} + g(q) = \tau, \quad (3)$$

$$x = f_{fwd}(q), \quad (4)$$

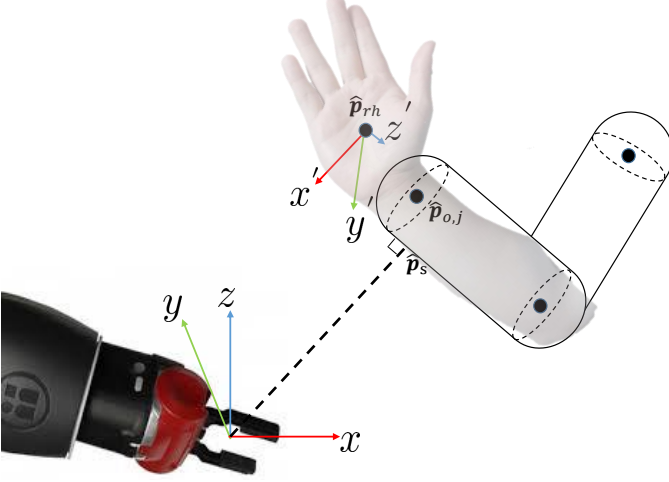


Figure 3: Calculation of the distance, position and orientation of the capsules for the representation of humans.

where $M(\mathbf{q}) \in \mathbb{R}^{n \times n}$ is a symmetric positive definite matrix, $\mathbf{C}(\mathbf{q}, \dot{\mathbf{q}}) \in \mathbb{R}^{n \times n}$ is a matrix of Coriolis and centrifugal forces terms, $\mathbf{g}(\mathbf{q}) \in \mathbb{R}^n$ is a vector of gravitational forces, $\mathbf{q} \in \mathbb{R}^7$ are the joint positions, and $f_{\text{fwd}} : \mathbb{R}^7 \rightarrow \mathbb{R}^3$ is the kinematic transformation from the joint angle positions \mathbf{q} to the Cartesian position of the end-effector $\mathbf{x} \in \mathbb{R}^3$. We consider the joint torque $\boldsymbol{\tau} \in \mathbb{R}^7$ as the system input and \mathbf{x} as the system output.

Defining $\mathbf{J} = \mathbf{J}(\mathbf{q}) = \frac{\partial f_{\text{fwd}}}{\partial \mathbf{q}}$ as the Jacobian matrix it follows that

$$\dot{\mathbf{x}} = \mathbf{J}(\mathbf{q})\dot{\mathbf{q}}, \quad (5a)$$

$$\ddot{\mathbf{x}} = \mathbf{J}(\mathbf{q})\ddot{\mathbf{q}} + \dot{\mathbf{J}}(\mathbf{q})\dot{\mathbf{q}}. \quad (5b)$$

By substituting (5a) into (3), the Cartesian robotic system dynamics can be expressed as

$$\mathbf{M}_x(\mathbf{q})\ddot{\mathbf{x}} + \mathbf{C}_x(\mathbf{q}, \dot{\mathbf{q}})\dot{\mathbf{x}} + \mathbf{g}_x(\mathbf{q}) = \mathbf{f}_h, \quad (6)$$

where $\mathbf{M}_x(\mathbf{q}) = \mathbf{J}^{\dagger\top} \mathbf{M}(\mathbf{q}) \mathbf{J}^{\dagger}$, $\mathbf{C}_x(\mathbf{q}, \dot{\mathbf{q}}) = \mathbf{J}^{\dagger\top} (\mathbf{C}(\mathbf{q}, \dot{\mathbf{q}}) - \mathbf{M}(\mathbf{q}) \mathbf{J}^{\dagger} \dot{\mathbf{J}}) \mathbf{J}^{\dagger}$, $\mathbf{g}_x(\mathbf{q}) = \mathbf{J}^{\dagger\top} \mathbf{g}(\mathbf{q})$ and $\mathbf{f}_h = \mathbf{J}^{\dagger} \boldsymbol{\tau}$ is the vector of generated control forces. $\mathbf{J}^{\dagger} = \mathbf{J}^{\dagger}(\mathbf{q})$ denotes the pseudo-inverse of $\mathbf{J}(\mathbf{q})$, that is:

$$\mathbf{J}^{\dagger}(\mathbf{q}) = (\mathbf{J}^{\top}(\mathbf{q}) \mathbf{J}(\mathbf{q}))^{-1} \mathbf{J}^{\top}(\mathbf{q}). \quad (7)$$

For notational simplicity, \mathbf{M}_x , \mathbf{C}_x , \mathbf{g}_x will be used to denote $\mathbf{M}_x(\mathbf{q})$, $\mathbf{C}_x(\mathbf{q}, \dot{\mathbf{q}})$, $\mathbf{g}_x(\mathbf{q})$, respectively. The system (2) is converted from joint space to task space, which can be expressed as

$$\begin{bmatrix} \dot{\mathbf{x}} \\ \ddot{\mathbf{x}} \end{bmatrix} = \underbrace{\begin{bmatrix} \dot{\mathbf{x}} \\ -\mathbf{M}_x^{-1}(\mathbf{C}_x \dot{\mathbf{x}} + \mathbf{g}_x) \end{bmatrix}}_{\mathbf{f}(\mathbf{x}, \dot{\mathbf{x}})} + \underbrace{\begin{bmatrix} 0 \\ -\mathbf{M}_x^{-1} \end{bmatrix}}_{\mathbf{g}(\mathbf{x})} \mathbf{f}_h, \quad (8)$$

Thus, the robotic system (8) is equivalent to the nonlinear affine system (2) with respect to the input \mathbf{f}_h . Therefore, the ECBF can be applied to the robotic system (8) to deal with the time-varying output constraints.

B. Minimum distance calculation

Achieving efficient and fast calculation of the minimum distance between humans and robots is vitally important for realizing safe human-robot interaction (HRI), where robots and human co-workers share the same workspace. The minimum distance is the main input for most collision avoidance, HRI, robot decision-making, and robot navigation methods [37]. Using the 32 3D joint coordinates provided by the skeletal tracking algorithm, bounding capsules (cylinders with semi-spherical ends) can be computed for the limbs, torso, and head as a simplified representation of the human in the distance calculation. We generate minimum bounding capsules along the bones in the skeleton, as shown in Fig.3. This is repeated for the predicted skeleton in each frame over the prediction horizon. For the 32 joint skeleton model representation $\hat{\mathbf{p}}_{\text{rh}}$ is the position of the center of the right hand.

We choose the capsules model to represent robot links since the computational load to compute the distance is low [38]. Each capsule is composed of a cylindrical part that encloses the link, while the joints at the extremities are enclosed in two semi-spheres. The 32 joint skeleton model, as used in the Human 3.6M dataset [39], maps to a total of 15 capsules for the human body. The approach to measure the distance between capsules is depicted in Fig.3. The distance calculation is implemented using the GJK (Gilbert-Johnson-Keerthi) algorithm [15]. The algorithm returns $\lambda(t)$ the minimum distance between the boundary of the capsules representing the human and the robot at time t .

C. Nonlinear model predictive control for collision avoidance

The robot's objective is for its end-effector to follow the estimated position of the human's right hand while avoiding collisions. To that end, we propose an NMPC formulation as a high-level control system that commands angular velocity references to a low-level control system (see Section VI-B). The overall controller architecture is shown in Fig. 4.

The input of the high-level control system is the joint velocity commands $\mathbf{u}(t)$. At every sampling time instant we need to solve a finite-horizon optimal control problem with prediction horizon $T_p > 0$, stage cost function ℓ and terminal cost function ℓ_f , where ℓ and ℓ_f are given by

$$\ell(\hat{\mathbf{x}}, \hat{\mathbf{u}}) = \mathbf{e}(\hat{\mathbf{p}}_{\text{rh}}, \hat{\mathbf{x}})^{\top} \mathbf{R}_p \mathbf{e}(\hat{\mathbf{p}}_{\text{rh}}, \hat{\mathbf{x}}) + \hat{\mathbf{u}}^{\top} \mathbf{R}_v \hat{\mathbf{u}}, \quad (9)$$

and

$$\ell_f(\hat{\mathbf{x}}) = \mathbf{e}(\hat{\mathbf{p}}_{\text{rh}}(T_p), \hat{\mathbf{x}}(T_p))^{\top} \mathbf{Q}_p \mathbf{e}(\hat{\mathbf{p}}_{\text{rh}}(T_p), \hat{\mathbf{x}}(T_p)) + \hat{\mathbf{u}}^{\top}(T_p) \mathbf{Q}_v \hat{\mathbf{u}}(T_p), \quad (10)$$

respectively. Here, $\mathbf{e}(\hat{\mathbf{p}}_{\text{rh}}(T_p), \mathbf{x}(t))$ is an error metric between the given Cartesian goal $\hat{\mathbf{p}}_{\text{rh}}(T_p)$ and current Cartesian state of the robot $\mathbf{x}(t)$. The reference position $\hat{\mathbf{p}}_{\text{rh}}(T_p)$ is obtained by the motion predictor. \mathbf{Q}_p and \mathbf{Q}_v are constant weight matrices for terms in the terminal cost function, while \mathbf{R}_p and \mathbf{R}_v

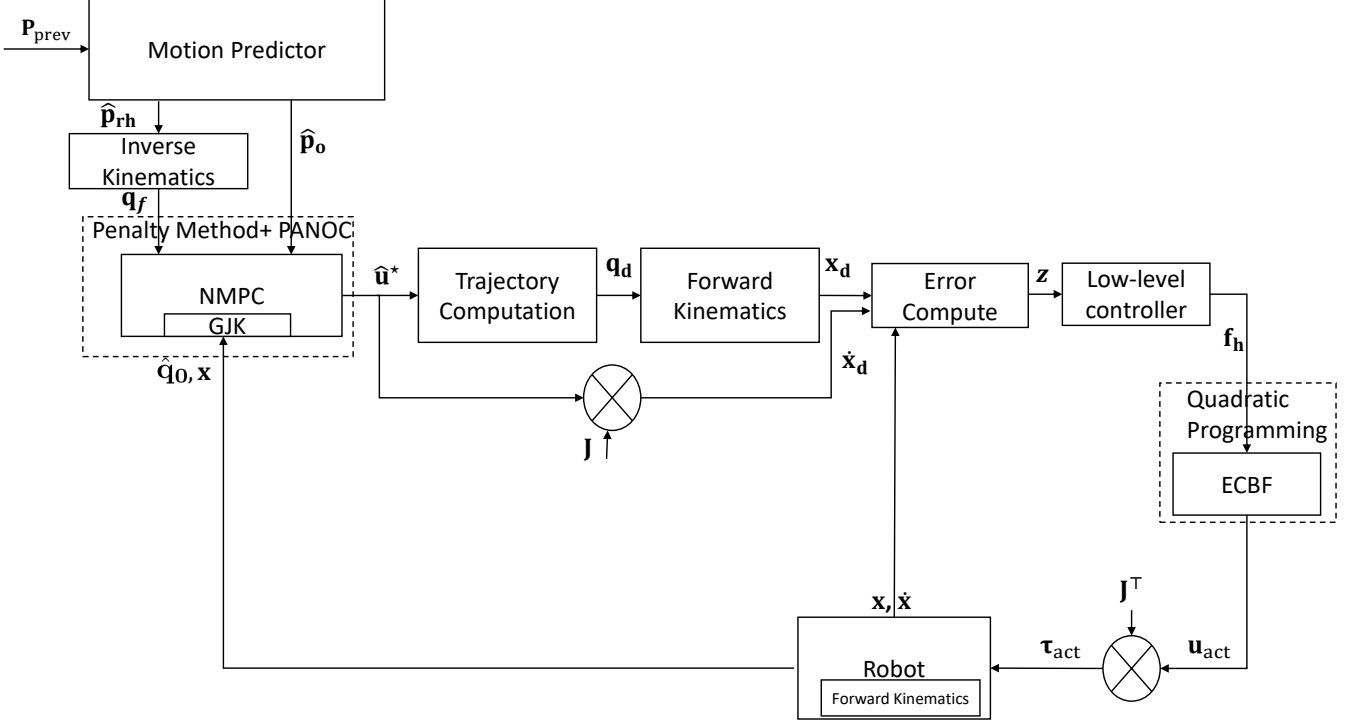


Figure 4: NMPC-based motion planning system

are the weight matrices for terms in the stage cost function. Following [40], the error function $e(\mathbf{x}_d, \hat{\mathbf{x}}(t))$ is defined as

$$e(\hat{\mathbf{p}}_{\text{rh}}(t), \mathbf{x}(t)) = \begin{bmatrix} -\mathbf{I}_3 & 0 \\ 0 & \mathbf{\Pi}_d \end{bmatrix} \hat{\mathbf{x}}(t) + \begin{bmatrix} \hat{\mathbf{p}}_{\text{rh}}(t) \\ 0 \end{bmatrix}, \quad (11)$$

where matrix $\mathbf{\Pi}_d$ is built from the desired quaternion, which remains constant during the optimization.

The initial and final configurations of the robot $\mathbf{q}_0 = [q_{01}, \dots, q_{07}]$ and $\mathbf{q}_f = [q_{f1}, \dots, q_{f7}]$ are obtained using the inverse kinematics function $\mathbf{f}_{\text{inv}} : \mathbb{R}^6 \rightarrow \mathbb{R}^7$, which converts the Cartesian end effector poses (position and orientation) to the corresponding joint positions. Using the GJK algorithm, the minimum distance calculation at time t is performed based on the Cartesian coordinates of the robot, $\mathbf{x}(t)$, and the predicted human pose, $\hat{\mathbf{p}}_o(t)$. The distance between the end-effector and the predicted operator's position $\lambda(\hat{\mathbf{x}}(t); \hat{\mathbf{p}}_o(t))$ is required to be greater than the minimum safe distance d_{safe} . The constraints are described as

$$\dot{\mathbf{q}}(t) = \hat{\mathbf{u}}(t), t \in [0, T_p], \quad (12a)$$

$$\hat{\mathbf{q}}(0) = \mathbf{q}_0, \quad (12b)$$

$$\hat{\mathbf{x}}(t) = \mathbf{f}_{\text{fwd}}(\hat{\mathbf{q}}(t)), t \in [0, T_p], \quad (12c)$$

$$\lambda(\hat{\mathbf{x}}(t); \hat{\mathbf{p}}_o(t)) \geq d_{\text{safe}}, t \in [0, T_p]. \quad (12d)$$

where $\mathbf{q} = (q_1, \dots, q_7)$ denotes the state of the robotic arm. The control actions are constrained in the set \mathcal{U} . Then, the

optimal solution $\hat{\mathbf{u}}^*$ is obtained by minimizing the optimal control cost function, that is,

$$\underset{\hat{\mathbf{x}}: [0, T_p] \rightarrow \mathcal{U}}{\text{minimize}} \ell_f(\hat{\mathbf{x}}(T_p)) + \int_0^{T_p} \ell(\hat{\mathbf{x}}(t), \hat{\mathbf{u}}(t)) dt, \quad (13)$$

subject to the constraints (12).

In this work we solve the NMPC problem using a numerical optimization method. To that end we convert the above problem to a discrete-time optimal control problem using an explicit discretisation and integration method. Assuming that $T_p = N_h T_s$, the NMPC problem in Equation (13) is reformulated to \mathbb{P}_d and depends on the current state \mathbf{q}_0 , the set-point \mathbf{q}_f for the joint positions, input \mathbf{u} and the estimated obstacle distance $\hat{\lambda}$ computed by the GJK algorithm as follows

$$\begin{aligned} \mathbb{P}_d(\hat{\mathbf{q}}_0, \hat{\mathbf{p}}_o, \mathbf{q}_f) : \underset{\hat{\mathbf{u}}_0, \dots, \hat{\mathbf{u}}_{N_h-1} \in \mathcal{U}}{\text{minimize}} \quad & \ell_{d,f}(\hat{\mathbf{x}}_{N_h}) \\ & + \sum_{k=0}^{N_h-1} \ell_d(\hat{\mathbf{x}}_k, \hat{\mathbf{u}}_k), \end{aligned} \quad (14a)$$

subject to the constraints

$$\hat{\mathbf{q}}_{k+1} = \hat{\mathbf{q}}_k + T_s \hat{\mathbf{u}}_k, k \in \mathbb{N}_{[0, N_h-1]}, \quad (14b)$$

$$\hat{\mathbf{q}}_0 = \mathbf{q}_0, \quad (14c)$$

$$\hat{\mathbf{q}}_{N_h} = \mathbf{q}_f, \quad (14d)$$

$$\hat{\mathbf{x}}_k = \mathbf{f}_{\text{fwd}}(\hat{\mathbf{q}}_k), k \in \mathbb{N}_{[0, N_h-1]}, \quad (14e)$$

$$\lambda(\hat{\mathbf{x}}_k; \hat{\mathbf{p}}_{o,k}) \geq d_{\text{safe}}, k \in \mathbb{N}_{[0, N_h-1]}. \quad (14f)$$

By solving \mathbb{P}_d at every discrete time instant, we obtain the solution $\hat{\mathbf{u}}_k^*$, $k \in \mathbb{N}_{[0, N_h-1]}$, only the first value of which,

$\hat{\mathbf{u}}_0^*$, is applied to the system and \mathbb{P}_d is solved again at the subsequent time instant in a receding horizon fashion.

D. Numerical solution

To solve \mathbb{P}_d numerically we employ OpEn [29], a code generation software package that generates optimizers in the Rust programming language for deployment on embedded devices. OpEn combines the PANOC numerical algorithm with the penalty method to solve the above problem. However, OpEn requires that we cast \mathbb{P}_d in the following general form

$$\underset{\mathbf{u} \in \tilde{\mathcal{U}}}{\text{minimize}} \quad F_0(\mathbf{u}), \quad (15a)$$

$$\text{subject to: } \mathbf{F}_i(\mathbf{u}) = \mathbf{0}, i \in \mathbb{N}_{[1, n_c]}, \quad (15b)$$

where $\mathbf{u} \in \mathbb{R}^n$ is the decision variable, $\tilde{\mathcal{U}} \subseteq \mathbb{R}^n$ is a nonempty closed set on which it is easy to compute projections, $F_0 : \mathbb{R}^n \rightarrow \mathbb{R}$ is a continuously differentiable cost function — not necessarily convex — with Lipschitz gradient, and $\mathbf{F}_i : \mathbb{R}^n \rightarrow \mathbb{R}^{m_i}$ are functions such that $\|\mathbf{F}_i\|^2$ is continuously differentiable with Lipschitz gradient.

To cast problem \mathbb{P}_d in this form, we choose the decision variable to be $\mathbf{u} = (\hat{\mathbf{u}}_0, \hat{\mathbf{u}}_1, \dots, \hat{\mathbf{u}}_{N-1})$ and define the sequence of functions

$$\Phi_{k+1}(\mathbf{u}, \mathbf{x}) = \begin{bmatrix} \mathbf{q}_0 + T_s \sum_{t=0}^k \mathbf{u}_t \\ \mathbf{f}_{\text{fwd}} \left(\mathbf{q}_0 + T_s \sum_{t=0}^k \mathbf{u}_t \right) \end{bmatrix} \quad (16)$$

with $\Phi_0(\mathbf{x}, \mathbf{u}) = [\mathbf{q}^\top \ \mathbf{x}^\top]^\top$. Note that $\Phi_{k+1}(\mathbf{u}, \mathbf{x})$ contains the location of the robot in both joint space and task space at time $k+1$ as a function of the initial state and the sequence of control actions \mathbf{u} . This allows us to eliminate the sequence of states and define the cost function

$$F_0(\mathbf{u}, \mathbf{x}) = \ell_{d,f}(\Phi_{N_h}(\mathbf{u}, \mathbf{x})) + \sum_{k=0}^{N_h-1} \ell_d(\Phi_k(\mathbf{u}, \mathbf{x}), \mathbf{u}_k). \quad (17)$$

In order to impose the terminal condition of Equation (14d) we define

$$\mathbf{F}_1(\mathbf{u}) = \hat{\mathbf{q}}_{N_h} - \mathbf{q}_f, \quad (18)$$

where $\hat{\mathbf{q}}_{N_h} = \hat{\mathbf{q}}_{N_h}(\mathbf{u}, \mathbf{x})$. To impose the obstacle avoidance condition of Equation (14f) we define

$$\mathbf{F}_{k+1}(\mathbf{u}) = [d_{\text{safe}} - \lambda(\Phi_k(\mathbf{u}, \mathbf{x}); \hat{\mathbf{p}}_{o,k})]_+, \quad (19)$$

for $k \in \mathbb{N}_{[0, N_h-1]}$. Lastly, we choose $\tilde{\mathcal{U}} = \mathcal{U}^{N_h}$ for the input constraints.

OpEn solves a series of optimization problems of the form

$$\mathbb{P}_{\text{in}} : \underset{\mathbf{u} \in U}{\text{minimize}} \quad F_0(\mathbf{u}) + c \sum_{i=1}^{n_c} \underbrace{\|\mathbf{F}_i(\mathbf{u})\|^2}_{\text{infeasibility}}, \quad (20)$$

for some $c > 0$ termed the *inner* problems. Essentially, the hard constraints of the original problem are turned into soft constraints. Starting with an initial value of c , a sequence of inner problems is solved numerically using the PANOC method while driving c to infinity and warm-starting each next inner problem with the solution of the previous one [29]. The algorithm terminates once the infeasibility, as defined in Equation (20) drops below a given tolerance $\epsilon_{\text{infeas}} > 0$.

VI. CONTROLLER DESIGN

A. Trajectory Computation

Given the estimated angular velocity command $\hat{\mathbf{u}}^*$, the desired joint state \mathbf{q}_d is updated as

$$\mathbf{q}_{d,k+1} = \mathbf{q}_{d,k} + T_s \hat{\mathbf{u}}^*. \quad (21)$$

Then, the generated desired joint position is used to calculate the desired Cartesian position \mathbf{x}_d and velocity $\dot{\mathbf{x}}_d$.

B. Low-level controller

In order to achieve asymptotic stability, the control force \mathbf{f}_h input to the safety filter is defined as

$$\mathbf{f}_h = \mathbf{C}_{\mathbf{x}}(\dot{\mathbf{x}}_d - \Lambda \tilde{\mathbf{x}}) + \mathbf{g}_{\mathbf{x}} + \mathbf{M}_{\mathbf{x}}(\ddot{\mathbf{x}}_d - \Lambda \dot{\tilde{\mathbf{x}}}) - k_z \text{sign}(\mathbf{z}), \quad (22)$$

where Λ and k_z are positive constants. A composite state error is denoted as $\mathbf{z} = \dot{\tilde{\mathbf{x}}} + \Lambda \tilde{\mathbf{x}}$, where $\tilde{\mathbf{x}} = \mathbf{x} - \mathbf{x}_d$ and $\dot{\tilde{\mathbf{x}}} = \dot{\mathbf{x}} - \dot{\mathbf{x}}_d$ are the error of the Cartesian position and velocity, respectively. $\text{sign}(\mathbf{z})$ is a sign function depends on the state error. Considering the chattering problem caused by the sign function, (22) is rewritten as

$$\mathbf{f}_h = \mathbf{C}_{\mathbf{x}}(\dot{\mathbf{x}}_d - \Lambda \tilde{\mathbf{x}}) + \mathbf{g}_{\mathbf{x}} + \mathbf{M}_{\mathbf{x}}(\ddot{\mathbf{x}}_d - \Lambda \dot{\tilde{\mathbf{x}}}) - k_z \frac{\mathbf{z}}{\|\mathbf{z}\| + c_1}, \quad (23)$$

where c_1 is a small positive number.

C. Exponential Control Barrier Function as a Safety Filter

In this section, an ECBF-based safety filter is introduced to prevent collisions with the human operator by constraining the trajectory generated by NMPC to be in a safe zone. ECBFs are formally defined as follows:

Definition 1 (ECBF [41]). Consider the system (8) and a set $\mathcal{C} = \{\mathbf{x} \in \mathbb{R}^3 \mid h(t, \mathbf{x}) \geq 0, \forall t > 0\}$ defined by a continuously differentiable function $h(t, \mathbf{x}) : \mathbb{R}^3 \rightarrow \mathbb{R}$ with relative degree $\kappa \geq 2$. Then $h(t, \mathbf{x})$ is an exponential control barrier function (ECBF) if there is a $\mathbf{k}_b \in \mathbb{R}^{\kappa-1}$ such that

$$\inf_{\mathbf{u} \in \mathcal{U}} [L_f^\kappa h(t, \mathbf{x}) + L_g L_f^{\kappa-1} h(t, \mathbf{x}) \mathbf{u} + \mathbf{k}_b \zeta_b(\mathbf{x})] \geq 0, \quad (24)$$

where ζ_b can be written as

$$\zeta_b(\mathbf{x}) := \begin{bmatrix} h(\mathbf{x}) \\ \dot{h}(\mathbf{x}) \\ \vdots \\ h^{(\kappa-1)}(\mathbf{x}) \end{bmatrix} = \begin{bmatrix} h(\mathbf{x}) \\ L_f h(\mathbf{x}) \\ \vdots \\ L_f^{(\kappa-1)} h(\mathbf{x}) \end{bmatrix}. \quad (25)$$

The method for selecting \mathbf{k}_b is detailed in [41]. The Lie derivative of $h(\mathbf{x})$ along $f(\mathbf{x})$ is defined as

$$L_f h(t, \mathbf{x}) = \frac{\partial h(t, \mathbf{x})}{\partial \mathbf{x}} f(\mathbf{x}, \dot{\mathbf{x}}), \quad (26)$$

where \mathbf{x} is the state of the system. The Lie derivative of $h(\mathbf{x})$ along $\mathbf{g}(\mathbf{x})$ is defined as $L_g h(t, \mathbf{x})$. Denote $\mathbf{p}_{oi}(t) \in \mathbb{R}^3$ as the

support point (i.e. a point on the boundary of the convex set that is closest to the robot) on the convex set representing the area of the human obstacle for the i^{th} robot joint computed by GJK at time t . To ensure the robot does not collide with the moving human, the Cartesian position of the robot joints $\mathbf{x}_i \in \mathbb{R}^3$, $i \in \mathbb{N}_{[1,7]}$ are under the following constraints

$$\|\mathbf{x}_i(t) - \hat{\mathbf{p}}_s(t)\|_2 > d_{\text{safe}}, \text{ for } i \in \mathbb{N}_{[1,7]}, t \geq 0, \quad (27)$$

where $\hat{\mathbf{p}}_s$ is a support point on the boundary of the capsule with the minimum distance to the i^{th} robot joint, as shown in Fig. 3. We define a candidate ECBF $h_i(t, \mathbf{x}_i)$ as

$$h_i(t, \mathbf{x}_i) = \|\mathbf{x}_i(t) - \hat{\mathbf{p}}_s(t)\|_2^2 - d_{\text{safe}}^2. \quad (28)$$

To modify the applied forces, \mathbf{f}_h , to guarantee safety, a quadratic programming (QP) based safety filter is employed. Considering the position constraints with relative degree 2, the optimization problem can be formulated as minimizing the normed difference between \mathbf{f}_h and the actual input \mathbf{u}_{act} , in order to maintain the robot within the safety region. In other words, $\mathbf{u}_{\text{act}}(\mathbf{x}, t)$ is the control input that minimizes the following QP

$$\underset{\mathbf{u}_{\text{act}} \in \mathcal{U}}{\text{minimize}} \|\mathbf{f}_h - \mathbf{u}_{\text{act}}\|^2, \quad (29a)$$

subject to

$$\begin{aligned} L_{\mathbf{f}}^2 h_i(t, \mathbf{x}) + L_{\mathbf{g}} L_{\mathbf{f}} h_i(t, \mathbf{x}) \mathbf{u}_{\text{act}} + k_1 h_i(t, \mathbf{x}) \\ + k_2 L_{\mathbf{f}} h_i(t, \mathbf{x}) \geq 0, i \in \mathbb{N}_{[1,7]}, \end{aligned} \quad (29b)$$

where $h_i(t, \mathbf{x})$ is as defined in (28). The robot joint torques are then obtained as $\boldsymbol{\tau}_{\text{act}} = \mathbf{J}^{\top}(\mathbf{q}) \mathbf{u}_{\text{act}}$. Further details on the implementation of ECBFs are given in [41].

D. System stability analysis

Proving the global stability of our ECBF-NMPC dynamic motion planning framework is challenging as it incorporates approximate numerical methods, a neural network based motion predictor, the GJK algorithm, and a safety filter. In order to guarantee local asymptotic stability, a control Lyapunov constraint is employed in the ECBF formulation and activated when the robot is close to the destination.

Property 1 [42]: The inertia matrix $\mathbf{M}(\mathbf{q})$ and $\mathbf{M}_{\mathbf{x}}$ are symmetric positive definite.

Property 2 [42]: The matrix $2\mathbf{C}_{\mathbf{x}}(\mathbf{q}, \dot{\mathbf{q}}) - \dot{\mathbf{M}}_{\mathbf{x}}(\mathbf{q})$ is skew-symmetric.

Definition 2 (\mathcal{K}_{∞} -class function [43]): A continuous function $\beta : \mathbb{R}_+ \rightarrow \mathbb{R}_+$ is a \mathcal{K}_{∞} -class function (denoted as $\beta \in \mathcal{K}_{\infty}$), if

- $\beta(0) = 0$
- β is increasing
- $\lim_{a \rightarrow \infty} \beta(a) = \infty$.

Definition 3 (Control Lyapunov Functions [44]): Given the system (8) and the composite error $\mathbf{z}(\mathbf{x}, t) = \dot{\mathbf{x}} + \Lambda \tilde{\mathbf{x}}$, with $\Lambda > 0$, consider a continuously differentiable function $V : \mathbb{R}^3 \rightarrow \mathbb{R}_+$ on set $\mathcal{Z} = \{\mathbf{z}(\mathbf{x}, t) \in \mathbb{R}^3 : \mathbf{x} \in \mathcal{C}, \forall t > 0\}$, where \mathcal{C} is the safe set as defined for the ECBF (Definition 1).

Then V is a control Lyapunov function (CLF) for the system in (8) if there exists $\beta_1, \beta_2, \beta_3 \in \mathcal{K}_{\infty}$ such that for all $\mathbf{z} \in \mathcal{Z}$

$$\beta_1(\|\mathbf{z}\|) \leq V(\mathbf{z}) \leq \beta_2(\|\mathbf{z}\|), \quad (30)$$

$$\inf_{\mathbf{u} \in \mathcal{U}} \dot{V}(\mathbf{z}, \mathbf{u}) \leq -\beta_3(\|\mathbf{z}\|). \quad (31)$$

The existence of a CLF implies the existence of a control law that renders the closed-loop system locally asymptotically stable [45, Thm. 2.5]. The target when employing a CLF constraint is to make the composite error $\mathbf{z}(\mathbf{x}, \dot{\mathbf{x}})$, which models the generalized Cartesian position and velocity errors with respect to the desired references, locally asymptotically converge to 0. Then, the problem (29) needs to satisfy both the ECBF and CLF constraints, which is written as

$$\underset{\mathbf{u}_{\text{act}} \in \mathcal{U}}{\text{minimize}} \|\mathbf{f}_h - \mathbf{u}_{\text{act}}\|^2, \quad (32a)$$

subject to

$$\begin{aligned} L_{\mathbf{f}}^2 h_i(t, \mathbf{x}_i) + L_{\mathbf{g}} L_{\mathbf{f}} h_i(t, \mathbf{x}_i) \mathbf{u}_{\text{act},i} + k_1 h_i(t, \mathbf{x}_i) \\ + k_2 L_{\mathbf{f}} h_i(t, \mathbf{x}_i) \geq 0, i \in \mathbb{N}_{[1,7]}, \end{aligned} \quad (32b)$$

$$\begin{aligned} \mathbf{z}_i^{\top} \left(\mathbf{u}_{\text{act},i} + k_z \frac{\mathbf{z}_i}{\|\mathbf{z}_i\| + c_1} \right) - \mathbf{z}_i^{\top} \mathbf{K}_D \mathbf{z}_i \geq 0, \\ i \in \mathbb{N}_{[1,7]}, \end{aligned} \quad (32c)$$

where \mathbf{K}_D is a symmetric positive definite matrix. The candidate Lyapunov function V is defined as

$$V(\mathbf{z}_i) = \frac{1}{2} \mathbf{z}_i^{\top} \mathbf{M}_{\mathbf{x}} \mathbf{z}_i. \quad (33)$$

Since $\mathbf{M}_{\mathbf{x}}(\mathbf{q})$ is positive definite for all \mathbf{q} , its minimum eigenvalue is positive. Assuming that $\inf_{\mathbf{q}} \lambda_{\min}(\mathbf{M}_{\mathbf{x}}(\mathbf{q})) > 0$ and $\sup_{\mathbf{q}} \lambda_{\max}(\mathbf{M}_{\mathbf{x}}(\mathbf{q})) < \infty$, the inequality in (30) is satisfied with $\beta_1(\|\mathbf{z}\|) = \inf_{\mathbf{q}} \lambda_{\min}(\mathbf{M}_{\mathbf{x}}(\mathbf{q})) \|\mathbf{z}\|^2$ and $\beta_2(\|\mathbf{z}\|) = \sup_{\mathbf{q}} \lambda_{\max}(\mathbf{M}_{\mathbf{x}}(\mathbf{q})) \|\mathbf{z}\|^2$.

Differentiating (33) with respect to time and using Property 1 to combine terms, gives

$$\dot{V} = \frac{1}{2} \mathbf{z}_i^{\top} \dot{\mathbf{M}}_{\mathbf{x}} \mathbf{z}_i + \mathbf{z}_i^{\top} \mathbf{M}_{\mathbf{x}} \dot{\mathbf{z}}_i \quad (34)$$

Noting that $\dot{\mathbf{z}}_i = \dot{\mathbf{x}}_i - \ddot{\mathbf{x}}_{d,i} + \Lambda(\dot{\mathbf{x}}_i - \dot{\mathbf{x}}_{d,i})$, and substituting for $\dot{\mathbf{M}}_{\mathbf{x}} \dot{\mathbf{x}}_i$ using (6) with \mathbf{f}_h replaced by the modified control force $\mathbf{f}_h - \mathbf{u}_{\text{act},i}$, $\mathbf{M}_{\mathbf{x}} \dot{\mathbf{z}}_i$ can be written as

$$\begin{aligned} \mathbf{M}_{\mathbf{x}} \dot{\mathbf{z}}_i = \mathbf{f}_h - \mathbf{u}_{\text{act},i} - \mathbf{C}_{\mathbf{x}}(\mathbf{z}_i + \dot{\mathbf{x}}_{d,i} \\ - \Lambda(\mathbf{x}_i - \mathbf{x}_{d,i})) - \mathbf{g}_{\mathbf{x}} - \mathbf{M}_{\mathbf{x}}(\ddot{\mathbf{x}}_{d,i} - \Lambda \dot{\mathbf{x}}_i) \end{aligned} \quad (35)$$

Substituting (35) into (34) yields

$$\begin{aligned} \dot{V} = \frac{1}{2} \mathbf{z}_i^{\top} \dot{\mathbf{M}}_{\mathbf{x}} \mathbf{z}_i + \mathbf{z}_i^{\top} [\mathbf{f}_h - \mathbf{u}_{\text{act},i} - \mathbf{C}_{\mathbf{x}}(\mathbf{z}_i + \dot{\mathbf{x}}_{d,i} \\ - \Lambda(\mathbf{x}_i - \mathbf{x}_{d,i})) - \mathbf{g}_{\mathbf{x}} - \mathbf{M}_{\mathbf{x}}(\ddot{\mathbf{x}}_{d,i} - \Lambda \dot{\mathbf{x}}_i)] \\ = \frac{1}{2} \mathbf{z}_i^{\top} (\dot{\mathbf{M}}_{\mathbf{x}} - 2\mathbf{C}_{\mathbf{x}}) \mathbf{z}_i + \mathbf{z}_i^{\top} [\mathbf{f}_h - \mathbf{u}_{\text{act},i} \\ - \mathbf{C}_{\mathbf{x}}(\dot{\mathbf{x}}_{d,i} - \Lambda \dot{\mathbf{x}}_i) - \mathbf{g}_{\mathbf{x}}] - \mathbf{z}_i^{\top} \mathbf{M}_{\mathbf{x}}(\ddot{\mathbf{x}}_{d,i} - \Lambda \dot{\mathbf{x}}_i). \end{aligned} \quad (36)$$

By Property 2, $\mathbf{z}_i^{\top} (\dot{\mathbf{M}}_{\mathbf{x}} - 2\mathbf{C}_{\mathbf{x}}) \mathbf{z}_i = 0$, hence the derivative of V can be expressed as

$$\begin{aligned} \dot{V} = \mathbf{z}_i^{\top} [(\mathbf{f}_h - \mathbf{u}_{\text{act},i}) - \mathbf{C}_{\mathbf{x}}(\dot{\mathbf{x}}_{d,i} - \Lambda \dot{\mathbf{x}}_i) - \mathbf{g}_{\mathbf{x}}] \\ - \mathbf{z}_i^{\top} \mathbf{M}_{\mathbf{x}}(\ddot{\mathbf{x}}_{d,i} - \Lambda \dot{\mathbf{x}}_i). \end{aligned} \quad (37)$$

Substituting (23) into (37) yields

$$\dot{V} = -\mathbf{z}_i^\top \mathbf{u}_{act,i} - \frac{k_z \mathbf{z}_i^\top \mathbf{z}_i}{\|\mathbf{z}_i\| + c_1}. \quad (38)$$

According to Definition 2 and (32c), the stability of the low-level controller is guaranteed when $\dot{V} \leq -\mathbf{z}_i^\top \mathbf{K}_D \mathbf{z}_i$ assuming problem (32) is feasible.

VII. EXPERIMENTAL SETUP

The collaboration scenario shown in Fig. 5 is a typical screw-driver usage scenario where the robot holding the screw at a random position, delivers it to the human operator before the operator picks the screw driver up. The operator's responsibility is to use the screw driver and take the screw from the robot end-effector, which stops at a safe interactive distance d_{safe} . The active collision avoidance is activated when the human body appears in the robot's original trajectory. For seamless human-robot collaboration, the robot starts to calculate a new trajectory based on the predicted future pose sequence for the operator (1 sec horizon, $N_h = 20$). Algorithm 1 shows the parameters and procedure for the screw-driver usage task.

Algorithm 1: Algorithm for vision-based screw-driver usage task

Input: f_{recg} (pretrained task classifier), f_{pred} (pretrained motion predictor), \mathbf{P}_{prev} (previous one second motion sequence), \mathbf{x} (current state of the robot).

Output: input to robot \mathbf{u}_{act}

Data: Stream data collected from OptiTrack

1 Define the controller.

2 **for** $t = 0, \dots, T_p$ **do**

3 $\hat{y} = f_{recg}(\mathbf{P}_{prev})$

4 **if** $\hat{y} \in \mathcal{A}_{int}$ **then**

5 $[\hat{p}_{rh}, \hat{p}_o] = f_{pred}(\mathbf{P}_{prev})$

6 Build the capsule-format human body and compute the minimum distance $\lambda(\mathbf{x}, \hat{p}_o)$.

7

8 Solve the defined problem in OpEn and compute the optimal input to the high-level controller $\hat{\mathbf{u}}^*$.

9 Compute the desired robot state \mathbf{q}_d and $\dot{\mathbf{q}}_d$.

10 Design the control input to the safety filter $f_h(t)$.

11 Solve the ECBF quadratic program to determine $\mathbf{u}_{act}(t)$.

12 Compute the input to the robot:

13 $\mathbf{u}_{act}(t) = \mathbf{J}^\top(\mathbf{q}(t)) \mathbf{u}_{act}(t)$.

14 Update the current state of the robot \mathbf{x}

15 Resample the previous one second motion $\bar{\mathbf{P}}_{prev}$.

16 $\mathbf{P}_{prev} \leftarrow \bar{\mathbf{P}}_{prev}$.

17 **end for**

A. Motion Capture

In this work, we generate high-quality skeleton data using an OptiTrack camera system. The volunteer performs the required behavior in a working environment with three cameras, with

the volunteer's behavior tracked from different perspectives, as shown in Fig 5(a). The human skeleton model generated has 32 joints, with joint data recorded at a sampling interval of 50 ms (i.e., 20 frames per second).

The capture space evaluated was based on typical use and had an extent of $2.5m \times 3.5m \times 2m = 17.5m^3$, an overview of which is given in Fig. 5. This space can be covered by 3 cameras. The number of cameras needed will increase for larger spaces (volumes). We have opted for a marker-based approach in this work, regardless of the high cost of system setup and calibration, to ensure high quality input into the perception system. For practical deployment marker-less systems may be more appropriate, and with recent advances in computer vision they are increasingly becoming a viable alternative to more expensive marker-based solutions [46]–[48].

B. Vision System

For the vision module, we use a non-local graph convolution (NGC) based method developed in [36] for action recognition and motion prediction. This implements a spatial-temporal attention mechanism to extract nonlocal spatial-temporal features enabling more accurate motion prediction over longer horizons than alternative approaches. As this model, referred to as the NGC-model, performs well for the Human 3.6M, CMU Mocap and NTU RGB-D datasets (see [36]), we repurpose it to predict the human motion associated with the screw-driver task and classify it into one of 5 subtasks that constitute the overall activity, namely, pick up, move forward, operate screw-driver, put down and break. This is achieved by retraining the network with a dataset collected for the screw-driver task consisting of skeletal data and associated subtask labels for three repetitions of the task. In this work, 4372 frames are used for training, while 1093 frames are used for testing. Each frame includes 3D joint positions with 32 joints, as well as ground-truth action labels for each frame.

1) Performance of the Vision Module: As shown by the confusion matrix in Fig. 6 (a), the model has a high prediction accuracy for each subtask (98.4%, 100%, 95.8%, 98.4% and 98.4%) and achieves an overall accuracy of 98%. For motion prediction, the Huber loss function is used to quantify the mean deviation between the predicted and actual locations of the human body joints in each frame. As shown in Fig. 6 (b), the NGC-model achieves the lowest error compared to selected baselines models from the literature (LSTM-3LR [49], Res-sup [50] and Traj-GCN [51]), with a final loss of 0.0141.

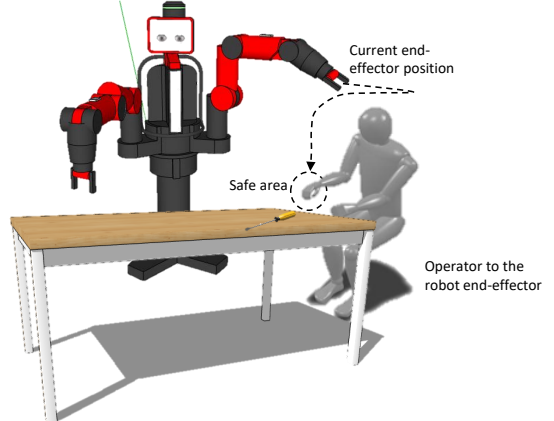
This shows that the proposed NCG-model can accurately and effectively identify the intended human body movement in real-time. Using this capability the HRC system can understand the intention of the human being when the human body is beginning an action, making it feasible for it to provide assistance to the human to complete the task efficiently.

C. Control System Performance Test

To evaluate NMPC-ECBF we implement it for a 7-DOF Baxter robot simulated in CoppeliaSim using a standard NMPC controller as a baseline comparison [12]. The system



(a)

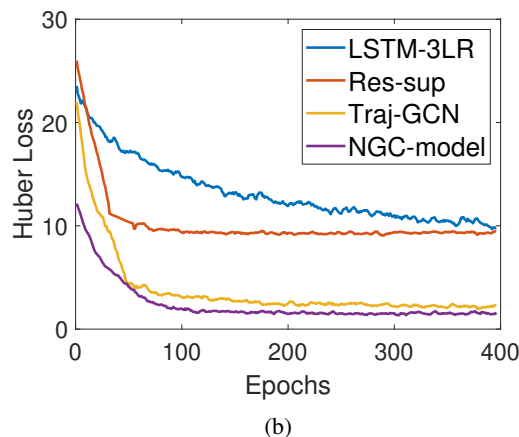


(b)

Figure 5: (a) Human dynamics tracking by OptiTrack cameras. (b) Collision-free human-robot collaboration scenario setup in a working environment.

	Pick up	0	1	1	0
Move Forward	2	211	2	0	1
Operate	0	0	235	0	1
Put Down	0	0	2	196	2
Break	0	0	1	1	231

(a)



(b)

Figure 6: (a) Confusion matrix describing the accuracy of action recognition in the screw-driver usage task. (b) Comparison of Huber loss obtained with different baseline models on collected dynamic data.

model employed in the MPC controller is discretized using the Euler method. The controller inputs are limited to $\pm 0.5 \text{ rad/s}$ for each joint. The weight matrices in ℓ and ℓ_f are selected as $\mathbf{Q}_v = \text{diag}(1,1,1,1,1,1)$, $\mathbf{Q}_p = \text{diag}(5,5,5,1,1,0)$, $\mathbf{R}_v = \text{diag}(0.1,0.1,0.1,0.1,0.1,0.1)$ and $\mathbf{R}_p = \text{diag}(3,3,3,0,0,0)$. Solution tolerances $\epsilon_a = 10^{-2}$ and $\epsilon_b = 10^{-4}$ are set for the fixed-point residual and the infeasibility, respectively. For the safety filter, safe set \mathcal{U} for input \mathbf{u}_{act} is $(-40 \text{ N}, 40 \text{ N})$. The parameters of the low-level controller are selected as $k_z = 5$ and $c_1 = 0.01$. The safe distance in our case is 10 cm. The ECBF coefficients k_b are chosen as [7, 7], while $\mathbf{K}_D = \text{diag}(5,5,5)$.

We design three scenarios to test collision avoidance and path planning performance. In the CoppeliaSim simulation, we model the movement of the human using the recorded trajectories of the skeleton joints. The Baxter robot starts from different initial positions and is required to reach the estimated position without collision with the simulated human. In scenario 1 the initial position of the robot is chosen to be close to the operator, as shown in Fig. 7 (a). In this extreme situation when the robot takes action, the possibility of a collision with the operator is high as the initial moving area for the robot is limited. In scenarios 2 and 3 the robot starts from two random positions in the workspace, where the initial position is far from the target (Fig. 8 (a) and (b)).

The initial position in scenario 2 is closer to the obstacles in the y-axis direction than in scenario 3. Scenario 1 is used to check if the safety filter can regulate the trajectory of the robot in the safe area, while scenarios 2 and 3 are designed to check if the ECBF can improve the path planning skill of NMPC.

The acceleration of the robot end-effector and the minimum distance between the robot and human obstacle during its motion in scenario 1 are plotted in Fig. 7 (b) and (c), respectively. The acceleration plot shows that NMPC-ECBF yields fewer abrupt changes in acceleration than the baseline NMPC path planner. The minimum distance plot highlights that the trajectory generated by NMPC violates the safe area

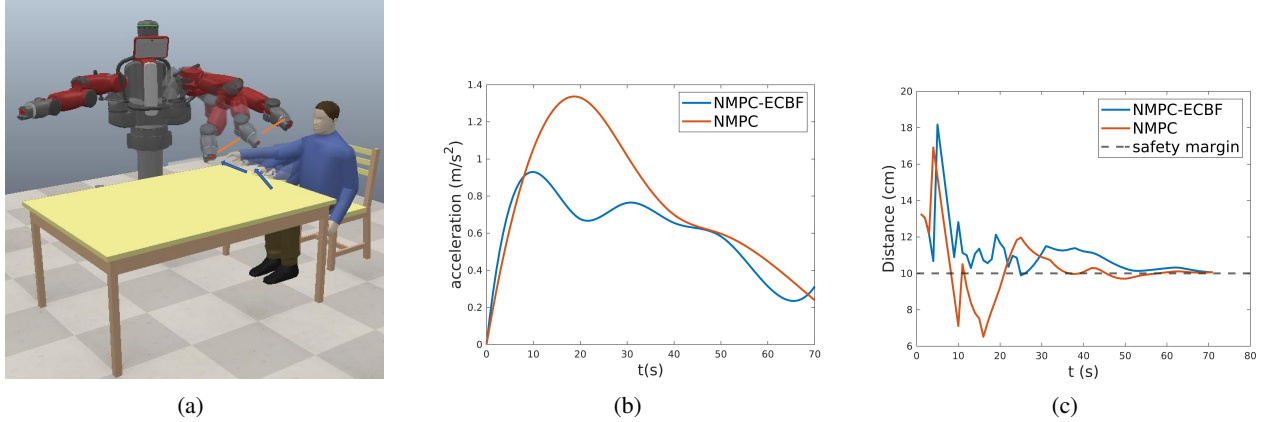


Figure 7: (a) HRC scenario when the initial position is close to the operator. (b) The acceleration of the end-effector. (c) The minimum distance to the obstacles among all the robot links.

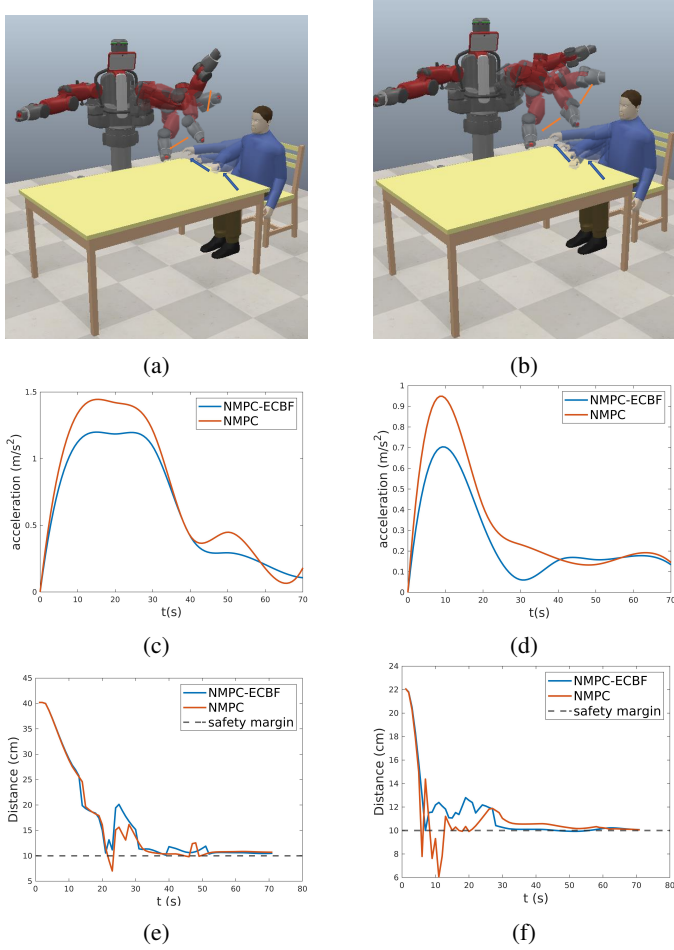


Figure 8: Comparison between NMPC (orange) and NMPC-ECBF (blue) for two different end-effector starting points: plots (a) and (b) show the trajectory of the robot end-effector from starting points 1 and 2, respectively; plots (c) and (d) show the acceleration of the end-effector; plots (e) and (f) show the corresponding evolution of the minimum Euclidean distance between the robot and human (obstacle).

at a number of points during the robot motion and that the inclusion of the ECBF safety filter has the desired effect of maintaining the motion within the safe area.

Fig. 8 plots the comparison of the performance of NMPC and NMPC-ECBF for scenarios 2 and 3. In these two scenarios, the initial position is comfortably outside the safe interactive area. The objective when comparing these two scenarios is to check if incorporating ECBF outperforms the trajectory generated by NMPC. The acceleration of the end-effector is plotted in Fig. 8(c) and (d) and the minimum distance between the end-effector and the safety margin for each case is shown in Fig. 8 (e) and (f). Noting that the safety margin was set as 10 cm in the experiments, NMPC-ECBF achieved constraint violation-free control for all scenarios considered, whereas the baseline controller violates the safety constraints at several points during the robot's motion. At the same time, NMPC-ECBF reduced peak acceleration by 17.2% and 26.3% in scenarios 2 and 3, respectively, compared to NMPC.

To further assess the robustness and reliability of the controller we perform 100 dynamic path planning HRC experiments with each one corresponding to a randomly generated robot start position and one of the 3 sets of human screwdriver usage task movement trajectories. For each experiment we recorded the maximum acceleration of the end-effector and the minimum distance between the end-effector and the target safety margin during the task execution. Table I reports the mean and most extreme values observed over the 100 experiments. The results show that NMCP-ECBF is able to strictly keep the robot motion within the safe area for all 100 simulations, with no violations of the safety margin ($d = 0$). In contrast, the NMPC path planner frequently breaches the safety margin, with an average violation of 1.9 cm and a maximum violation of 4.2 cm. Furthermore, NMPC-ECBF outperforms NMPC in terms of the average and maximum joint accelerations, achieving a reduction in these values of 17.6% and 15.5%, respectively.

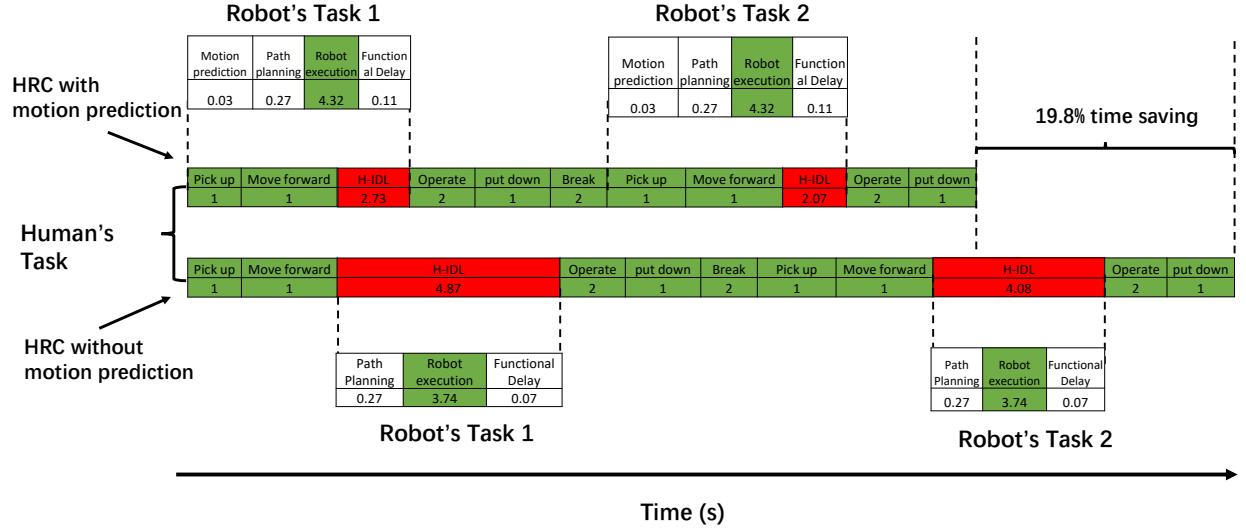


Figure 9: Task assignment chart for the baseline approach of strict turn taking, where each action is immediately followed by the next action of the other teammate.

Table I: Controller performance for 100 HRC task instances.

	max acc (m/s^2)	min d (cm)	avg max acc (m/s^2)	avg min d (cm)
NMPC	1.61	-4.2	1.48	-1.9
NMPC-ECBF	1.36	0	1.22	0

D. Idle time for agents in the HRC scenario

Fig. 9 compares the human idle time (H-IDL) and robot idle time (R-IDL) in the screw-driver usage HRC task to highlight the benefit of integrating motion prediction into HRC. In the proposed screw-driver usage task, the original length of this HRC task is 12 seconds, which is the time used in human-human collaboration. Red blocks indicate when the operator is in an idle state, waiting for the screw to arrive. Blue blocks are the times the robot is idle for computation and data loading. Green blocks are the times when both agents are executing the commanded task. The R-IDL when employing motion prediction based control consists of the time for motion prediction, path planning, functional delay and the time before the robot is triggered again. Here the functional delay is caused by data and function loading. H-IDL in this scenario takes 29% of the total time. It is obvious that robot execution time takes the majority of the total (i.e. 4.32/4.73 for R-task1 and 3.69/4.07 for R-task2) when employing the motion predictor and embedded optimization engine. In this way, we can achieve a H-IDL rate of 29% and a R-IDL rate of 53% in the HRC task.

In the HRC task implemented without motion prediction, the robot has to start path planning after the human operator moves their right hand to the target interactive position. Table. II shows a comparison between human idle time (H-IDL) and robot idle time (R-IDL) in the designed human-robot collaboration tasks. The H-IDL rate and R-IDL rate are 43% and 57%, respectively, without motion prediction. Therefore, motion prediction reduces the idle time for both agents in the HRC task. As a result, the total execution time is reduced from

20.95 to 16.80 seconds, a saving of 19.8%.

Table II: Comparison of the idle time between the tasks with or without motion prediction.

	With Motion Prediction (s)	Without Motion Prediction (s)	Total Time
H-IDL	4.80	8.95	16.80
R-IDL	8.89	12.00	20.95

VIII. CONCLUSIONS

The proposed NMPC-ECBF control framework allows a robot to safely re-plan its motion in the presence of a human, delivering smooth acceleration and adaptivity in the presence of uncertainty. The results demonstrate the necessity of adding a safety filter into the NMPC controller in the trajectory planning problem. This represents a promising approach for manufacturing applications due to its characteristic of providing a strict constraint on robot motion. In addition, by employing human motion prediction within the framework tasks can be executed more efficiently with a lower idle rate achievable for both agents in a HRC task than with traditional turn-taking task execution.

Future work will be devoted to testing the proposed algorithm when there is uncertainty regarding the system dynamics (e.g., caused by joint friction). The possibility of using robust NMPC to account for imperfect tracking of the predicted NMPC trajectory will also be investigated. In addition, we will also explore the applicability of our approach to scenarios involving both physical and non-physical HRC interactions, with the robot switching between different control modes based on the prevailing circumstances, as determined by a higher-level supervisory system.

REFERENCES

- [1] M. L. Nicora, R. Ambrosetti, G. J. Wiens, and I. Fassi, “Human–robot collaboration in smart manufacturing: Robot reactive behavior intelligence”, *Journal of Manufacturing Science and Engineering*, vol. 143, no. 3, 2021.
- [2] C. Qian, Y. Zhang, C. Jiang, S. Pan, and Y. Rong, “A real-time data-driven collaborative mechanism in fixed-position assembly systems for smart manufacturing”, *Robotics and Computer-Integrated Manufacturing*, vol. 61, p. 101 841, 2020.
- [3] R. Triebel, K. Arras, R. Alami, *et al.*, “Spencer: A socially aware service robot for passenger guidance and help in busy airports”, in *Field and service robotics*, Springer, 2016, pp. 607–622.
- [4] S. Proia, R. Carli, G. Cavone, and M. Dotoli, “Control techniques for safe, ergonomic, and efficient human–robot collaboration in the digital industry: A survey”, *IEEE Transactions on Automation Science and Engineering*, 2021.
- [5] W. Wang, R. Li, Y. Chen, Z. M. Diekel, and Y. Jia, “Facilitating human–robot collaborative tasks by teaching-learning-collaboration from human demonstrations”, *IEEE Transactions on Automation Science and Engineering*, vol. 16, no. 2, pp. 640–653, 2018.
- [6] Q. Lei, J.-X. Du, H.-B. Zhang, S. Ye, and D.-S. Chen, “A survey of vision-based human action evaluation methods”, *Sensors*, vol. 19, no. 19, p. 4129, 2019.
- [7] W. Wang, R. Li, Y. Chen, Y. Sun, and Y. Jia, “Predicting human intentions in human–robot hand-over tasks through multimodal learning”, *IEEE Transactions on Automation Science and Engineering*, 2021.
- [8] V. Villani, F. Pini, F. Leali, and C. Secchi, “Survey on human–robot collaboration in industrial settings: Safety, intuitive interfaces and applications”, *Mechatronics*, vol. 55, pp. 248–266, 2018.
- [9] S. Ide, T. Takubo, K. Ohara, Y. Mae, and T. Arai, “Real-time trajectory planning for mobile manipulator using model predictive control with constraints”, in *2011 8th International Conference on Ubiquitous Robots and Ambient Intelligence (URAI)*, IEEE, 2011, pp. 244–249.
- [10] M. Salaj, M. Gulani, *et al.*, “Pendubot control scheme based on nonlinear mpc and mhe exploiting parallelization”, in *2015 IEEE 19th International Conference on Intelligent Engineering Systems (INES)*, IEEE, 2015, pp. 353–358.
- [11] W. Li and R. Xiong, “Dynamical obstacle avoidance of task-constrained mobile manipulation using model predictive control”, *IEEE Access*, vol. 7, pp. 88 301–88 311, 2019.
- [12] A. Oleinikov, S. Kusdavletov, A. Shintemirov, and M. Rubagotti, “Safety-aware nonlinear model predictive control for physical human–robot interaction”, *IEEE Robotics and Automation Letters*, vol. 6, no. 3, pp. 5665–5672, 2021.
- [13] J. Rawlings, D. Mayne, and D. M.M., *Model Predictive Control: Theory, Computation, and Design*, 4th. Nob Hill Publishing, 2022.
- [14] I. J. Wolf and W. Marquardt, “Fast nmpc schemes for regulatory and economic nmpc—a review”, *Journal of Process Control*, vol. 44, pp. 162–183, 2016.
- [15] S. Secil and M. Ozkan, “Minimum distance calculation using skeletal tracking for safe human–robot interaction”, *Robotics and Computer-Integrated Manufacturing*, vol. 73, p. 102 253, 2022.
- [16] H. Wang, J. Peng, F. Zhang, H. Zhang, and Y. Wang, “High-order control barrier functions-based impedance control of a robotic manipulator with time-varying output constraints”, *ISA transactions*, 2022.
- [17] T. D. Son and Q. Nguyen, “Safety-critical control for non-affine nonlinear systems with application on autonomous vehicle”, in *2019 IEEE 58th Conference on Decision and Control (CDC)*, IEEE, 2019, pp. 7623–7628.
- [18] C. Wang, Y. Meng, Y. Li, S. L. Smith, and J. Liu, “Learning control barrier functions with high relative degree for safety-critical control”, in *2021 European Control Conference (ECC)*, IEEE, 2021, pp. 1459–1464.
- [19] H. Liu and L. Wang, “Human motion prediction for human–robot collaboration”, *Journal of Manufacturing Systems*, vol. 44, pp. 287–294, 2017.
- [20] Z. Liu, Q. Liu, W. Xu, Z. Liu, Z. Zhou, and J. Chen, “Deep learning-based human motion prediction considering context awareness for human–robot collaboration in manufacturing”, *Procedia CIRP*, vol. 83, pp. 272–278, 2019.
- [21] B. Lindqvist, S. S. Mansouri, A.-a. Agha-mohammadi, and G. Nikolakopoulos, “Nonlinear mpc for collision avoidance and control of uavs with dynamic obstacles”, *IEEE robotics and automation letters*, vol. 5, no. 4, pp. 6001–6008, 2020.
- [22] B. Lindqvist, S. S. Mansouri, C. Kanellakis, and G. Nikolakopoulos, “Collision free path planning based on local 2d point-clouds for mav navigation”, in *2020 28th Mediterranean Conference on Control and Automation (MED)*, IEEE, 2020, pp. 538–543.
- [23] A. Wächter and L. T. Biegler, “On the implementation of an interior-point filter line-search algorithm for large-scale nonlinear programming”, *Mathematical programming*, vol. 106, no. 1, pp. 25–57, 2006.
- [24] D. B. Leineweber, A. Schäfer, H. G. Bock, and J. P. Schlöder, “An efficient multiple shooting based reduced sqp strategy for large-scale dynamic process optimization: Part ii: Software aspects and applications”, *Computers & chemical engineering*, vol. 27, no. 2, pp. 167–174, 2003.
- [25] B. Houska, H. J. Ferreau, and M. Diehl, “An auto-generated real-time iteration algorithm for nonlinear mpc in the microsecond range”, *Automatica*, vol. 47, no. 10, pp. 2279–2285, 2011.
- [26] J. L. Jerez, P. J. Goulart, S. Richter, G. A. Constantinides, E. C. Kerrigan, and M. Morari, “Embed-

ded online optimization for model predictive control at megahertz rates”, *IEEE Transactions on Automatic Control*, vol. 59, no. 12, pp. 3238–3251, 2014.

[27] A. Sathya, P. Sopasakis, R. Van Parys, A. Themelis, G. Pipeleers, and P. Patrinos, “Embedded nonlinear model predictive control for obstacle avoidance using panoc”, in *2018 European control conference (ECC)*, IEEE, 2018, pp. 1523–1528.

[28] L. Stella, A. Themelis, P. Sopasakis, and P. Patrinos, “A simple and efficient algorithm for nonlinear model predictive control”, in *2017 IEEE 56th Annual Conference on Decision and Control (CDC)*, IEEE, 2017, pp. 1939–1944.

[29] P. Sopasakis, E. Fresk, and P. Patrinos, “Open: Code generation for embedded nonconvex optimization”, *IFAC-PapersOnLine*, vol. 53, no. 2, pp. 6548–6554, 2020.

[30] S. Trimble, W. Naeem, S. McLoone, and P. Sopasakis, “Context-aware robotic arm using fast embedded model predictive control”, in *2020 31st Irish Signals and Systems Conference (ISSC)*, IEEE, 2020, pp. 1–6.

[31] M. Rubagotti, P. Patrinos, and A. Bemporad, “Stabilizing linear model predictive control under inexact numerical optimization”, *IEEE Transactions on Automatic Control*, vol. 59, no. 6, pp. 1660–1666, 2014. DOI: 10.1109/TAC.2013.2293451.

[32] T. Gurriet, M. Mote, A. Singletary, P. Nilsson, E. Feron, and A. D. Ames, “A scalable safety critical control framework for nonlinear systems”, *IEEE Access*, vol. 8, pp. 187249–187275, 2020.

[33] Q. Nguyen and K. Sreenath, “Robust safety-critical control for dynamic robotics”, *IEEE Transactions on Automatic Control*, 2021.

[34] A. Singletary, S. Kolathaya, and A. D. Ames, “Safety-critical kinematic control of robotic systems”, *IEEE Control Systems Letters*, vol. 6, pp. 139–144, 2021.

[35] C. T. Landi, F. Ferraguti, S. Costi, M. Bonfè, and C. Secchi, “Safety barrier functions for human-robot interaction with industrial manipulators”, in *2019 18th European Control Conference (ECC)*, IEEE, 2019, pp. 2565–2570.

[36] D. Zhang, N. A. Vien, M. Van, and S. McLoone, “Non-local graph convolutional network for joint activity recognition and motion prediction”, in *2021 IEEE/RSJ International Conference on Intelligent Robots and Systems (IROS)*, IEEE, 2021, pp. 2970–2977.

[37] M. Safeea, N. Mendes, and P. Neto, “Minimum distance calculation for safe human robot interaction”, *Procedia Manufacturing*, vol. 11, pp. 99–106, 2017.

[38] H.-C. Lin, C. Liu, Y. Fan, and M. Tomizuka, “Real-time collision avoidance algorithm on industrial manipulators”, in *2017 IEEE Conference on Control Technology and Applications (CCTA)*, IEEE, 2017, pp. 1294–1299.

[39] C. Ionescu, D. Papava, V. Olaru, and C. Sminchisescu, “Human3. 6m: Large scale datasets and predictive methods for 3d human sensing in natural environments”, *IEEE transactions on pattern analysis and machine intelligence*, vol. 36, no. 7, pp. 1325–1339, 2013.

[40] S. Hu, E. Babaian, M. Karimi, and E. Steinbach, “Nmpc-mp: Real-time nonlinear model predictive control for safe motion planning in manipulator teleoperation”, in *2021 IEEE/RSJ International Conference on Intelligent Robots and Systems (IROS)*, IEEE, 2021, pp. 8309–8316.

[41] Q. Nguyen and K. Sreenath, “Exponential control barrier functions for enforcing high relative-degree safety-critical constraints”, in *2016 American Control Conference (ACC)*, IEEE, 2016, pp. 322–328.

[42] W. He, S. S. Ge, Y. Li, E. Chew, and Y. S. Ng, “Neural network control of a rehabilitation robot by state and output feedback”, *Journal of Intelligent & Robotic Systems*, vol. 80, no. 1, pp. 15–31, 2015.

[43] R. Grandia, A. J. Taylor, A. Singletary, M. Hutter, and A. D. Ames, “Nonlinear model predictive control of robotic systems with control lyapunov functions”, *arXiv preprint arXiv:2006.01229*, 2020.

[44] M. V. Minniti, R. Grandia, F. Farshidian, and M. Hutter, “Adaptive clf-mpc with application to quadrupedal robots”, *IEEE Robotics and Automation Letters*, vol. 7, no. 1, pp. 565–572, 2021.

[45] E. D. Sontag, “A lyapunov-like characterization of asymptotic controllability”, *SIAM Journal on Control and Optimization*, vol. 21, no. 3, pp. 462–471, 1983. DOI: 10.1137/0321028.

[46] A. S. Ebrahimi, P. Orlowska-Feuer, Q. Huang, et al., “Three-dimensional unsupervised probabilistic pose reconstruction (3d-upper) for freely moving animals”, *Scientific Reports*, vol. 13, no. 1, p. 155, 2023.

[47] V. Bazarevsky, I. Grishchenko, K. Raveendran, T. Zhu, F. Zhang, and M. Grundmann, “Blazepose: On-device real-time body pose tracking”, *arXiv preprint arXiv:2006.10204*, 2020.

[48] A. Mathis, P. Mamidanna, K. M. Cury, et al., “Deeplabcut: Markerless pose estimation of user-defined body parts with deep learning”, *Nature Neuroscience*, 2018. [Online]. Available: <https://www.nature.com/articles/s41593-018-0209-y>.

[49] L.-Y. Gui, K. Zhang, Y.-X. Wang, X. Liang, J. M. Moura, and M. Veloso, “Teaching robots to predict human motion”, in *2018 IEEE/RSJ International Conference on Intelligent Robots and Systems (IROS)*, IEEE, 2018, pp. 562–567.

[50] J. Martinez, M. J. Black, and J. Romero, “On human motion prediction using recurrent neural networks”, in *Proceedings of the IEEE Conference on Computer Vision and Pattern Recognition*, 2017, pp. 2891–2900.

[51] W. Mao, M. Liu, M. Salzmann, and H. Li, “Learning trajectory dependencies for human motion prediction”, in *Proceedings of the IEEE/CVF International Conference on Computer Vision*, 2019, pp. 9489–9497.